Numerical analysis of the effect of the scan strategy on the residual stress in the multi-laser selective laser melting

Zou, Sheng; Xiao, Hanbin; Ye, Fangping; Li, Zongchen; Tang, Wenzhi; Zhu, Feng; Chen, Chentong; Zhu, Chao

DOI
10.1016/j.rinp.2020.103005

Publication date
2020

Document Version
Final published version

Published in
Results in Physics

Results in Physics 16 (2020) 103005

Contents lists available at ScienceDirect

Results in Physics

journal homepage: www.elsevier.com/locate/rinp

Numerical analysis of the effect of the scan strategy on the residual stress in the multi-laser selective laser melting

Sheng Zou[a], Hanbin Xiao[a], Fangping Ye[b,*], Zongchen Li[c], Wenzhi Tang[a], Feng Zhu[a], Chentong Chen[a], Chao Zhu[a]

[a] School of Logistics Engineering, Wuhan University of Technology, Wuhan 430063, China
[b] School of Mechanical Engineering, Hubei University of Technology, Wuhan 430068, China
[c] Department of Maritime and Transport Technology, Delft University of Technology, 2628 CD Delft, the Netherlands

ARTICLE INFO

Keywords:
Selective laser melting
Multi-laser
Thermo-mechanical model
Residual stress
Scan strategy

ABSTRACT

The inevitably formed residual stress in the Selective Laser Melting (SLM) process leads to distortion, crack and even delamination of the workpiece. Single laser is commonly applied during SLM processing. However, its productivity is much lower than multiple lasers. In addition, the research of residual stress with multi-laser condition currently is limited in the open documents. In this paper, a three-dimensional (3D) thermo-mechanical model, with considerations of temperature dependent properties of Ti-6Al-4V, phase change and convective flow, is developed at first. Then, the numerical results of maximum temperature and dimensions of the molten pool are validated by available experimental data. Furthermore, a parametric study in regards to a series of scan strategies is investigated. According to the simulation results, the residual stress increases significantly when the laser number reaches four. The "two-zone technique" scan strategy decreases the equivalent residual stress by 10.6% compared to the successive scan strategy. With a shortening scan length, the residual stress first increases slightly, then decreases dramatically and attains the minimum when it is a quarter. Furthermore, for the multi-laser SLM process, carefully planning the scanning sequence and the sweeping direction to decrease heat concentration is beneficial in controlling the residual stress.

Introduction

Selective Laser Melting (SLM), as a promising Additive Manufacturing (AM) technology, is widely used in aerospace, biomedical, mold manufacturing and other industries in recent years [1–3]. The near-net-shape, geometrically complex and high-density metallic structures can be fabricated using this technology within a short design and manufacture cycle [4,5]. Due to the factor of rapid heating and cooling in the SLM processing, residual stresses are often inevitably generated in the deposited layers and substrate that leads to the distortion, crack and even delamination of the workpiece [6–8]. Therefore, it is of significance to investigate the mechanism of how SLM processing conditions affect the residual stress and then optimize the process parameters to control the residual stress. However, the experimental measurement of residual stress is expensive and time consuming. And the accuracy of the results depends on the dimension and precision of the workpiece and the accuracy of X-ray [9]. Moreover, the three-dimensional (3D) transient temperature field in the SLM processing cannot be obtained using thermocouple and infrared thermography [10,11]. The validated numerical simulation method is an effective alternative for evaluating the temperature field and the residual stress field.

Previously, researchers have developed numerical models to simulate the AM process [12,13]. Xinran et al. [14] developed a 3D transient model to investigate the thermo-mechanical response of Ti-6Al-4V part, but the accelerated heat transfer resulted from the convective flow within the molten pool was not taken into consideration. Mohammad et al. [15] and K. Ren et al. [16] increased the thermal conductivity of liquid metal to minimize temperature errors, while the convective flow is not considered. This leads to the calculated molten pool dimension inconsistent with the reality. A thermo-mechanical model coupled Finite Volume Method (FVM) with finite element method (FEM) was developed to predict temperature and residual stress distribution of the thin wall fabricated by laser cladding method [17]. Although the calculation results agree well with the experimental results, the thermal properties of powders are not considered in this simulation. Therefore, an integrated therm-mechanical model which taking consideration of reasonable heat source, convective flow, phase change, variable

* Corresponding author.
E-mail address: yefangping@whut.edu.cn (F. Ye).

https://doi.org/10.1016/j.rinp.2020.103005
Received 13 November 2019; Received in revised form 22 January 2020; Accepted 9 February 2020
Available online 12 February 2020

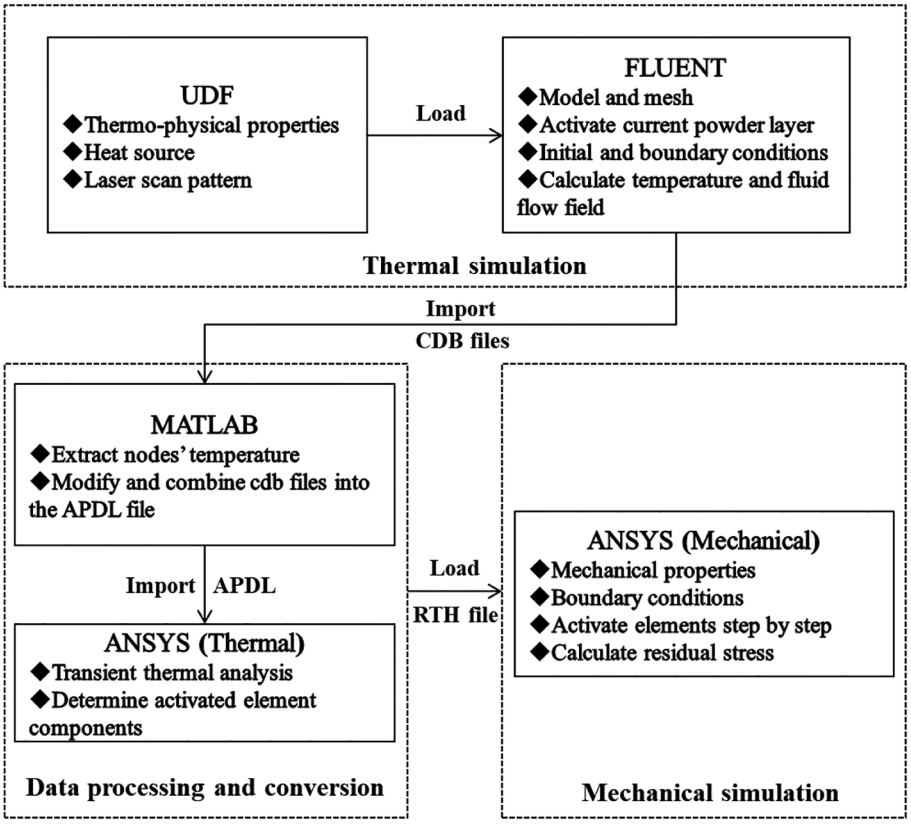

Fig.1. The workflow of the thermo-mechanical model.

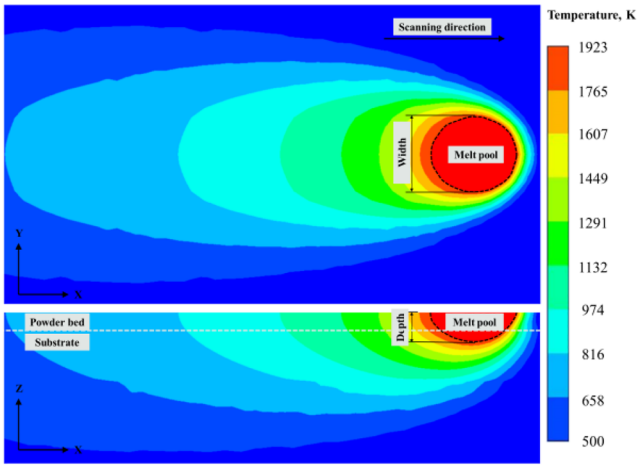

Fig.2. The temperature distribution and dimensions of the melt pool for 50 W laser power, 200 mm/s scanning speed and 30 μm powder layer thickness.

Table 1
SLM processing parameters used in simulation.

Parameters (unit)	Nomenclature	Value
Average particle diameter (μm)	D_p	16.6 [32]
Powder layer thickness (μm)	L_p	30 [34]
Powder bed porosity	ϕ	0.4 [15]
Laser radius (μm)	r_0	35 [32]
Laser power (W)	P	50 [32]
Scanning speed (mm/s)	v_l	100, 125, 200, 250, 300 [32,34]
Laser absorption	A_p	0.47
Attenuation coefficient	A_z	5×10^4
Laser distribution coefficient	d	0.5 [28]
Emissivity	ε_{pd}	0.35 [38]
Ambient temperature (K)	T_∞	300
Convective coefficient($W{\cdot}m^{-2}{\cdot}K^{-1}$)	h_{conv}	10 [35]
Argon thermal conductivity ($W{\cdot}m^{-1}{\cdot}K^{-1}$)	k_g	0.0173

thermal and mechanical properties, is still in a great demand, in order to accurately simulate the SLM process.

The scan strategy is critical for the formation of residual stress in the final workpiece and researchers have investigated the influence of scan strategy on residual stresses [18–21]. Cheng et al. [22] analyzed the effects of six different scan patterns on material temperature distribution, stresses and deformations, and found that the component using 45 degrees inclined scanning method had the smallest residual stresses and distortions. Ali et al. [23] experimentally measured residual stresses in SLM Ti-6Al-4V parts and concluded that rotating scanning direction 90 degrees for each layer was conducive to reduce residual stress. Parry et al. [12] and Wu et al. [24] drew the same conclusion that reducing the length of the scan vector was effective in reducing residual stress. However, Lu et al. [25] experimentally measured four SLM parts using 2 × 2 mm, 3 × 3 mm, 5 × 5 mm and 7 × 7 mm island scan strategies, and found that 3 × 3 mm scan length led to the highest residual stress. Thus, understanding the influence of scan strategy on the residual stress is still of great value.

In order to improve the productivity of the small-size SLM part, multiple lasers are introduced to decrease the time for laser scanning and depositing/removing powder [15]. With the multi-laser scan strategy development, the SLM process becomes dramatically complicated [26–27]. Unfortunately, the effect of multi-laser scan strategy on residual stresses has not been clearly revealed. Thus, in this paper, a thermo-mechanical model of the SLM process is presented to investigate the effect of scan strategy for single laser and multiple lasers on the residual stress, with consideration of temperature, phase dependent properties, phase change and convective flow. First, the

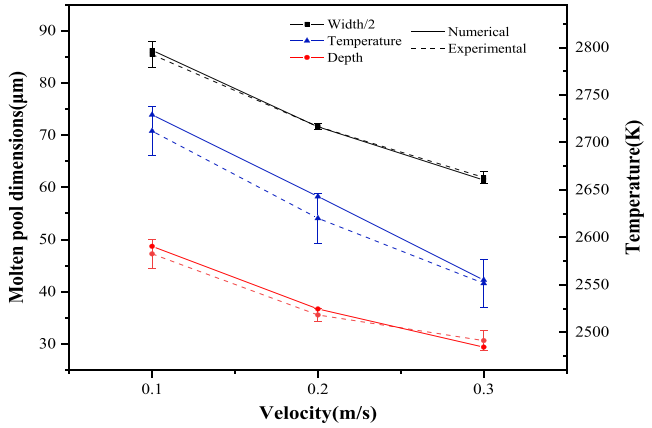

Fig. 3. The calculated and experimentally measured depth and half of width of molten pools and maximum temperatures versus scanning speed of laser.

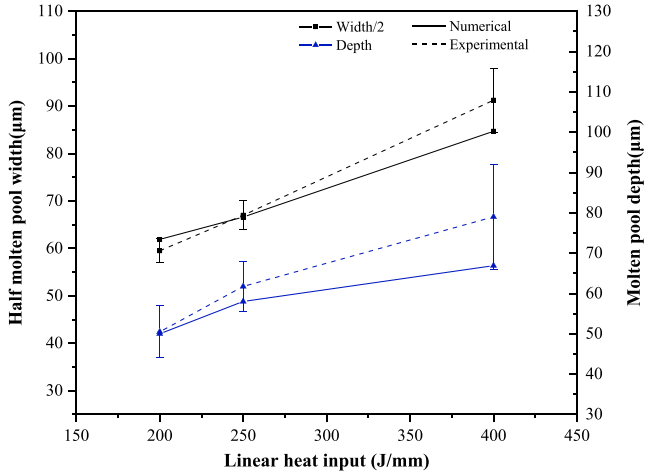

Fig. 4. Comparison of the molten pool dimensions obtained from simulation and experiment as the linear heat input heat increase from 200 J/mm to 400 J/mm.

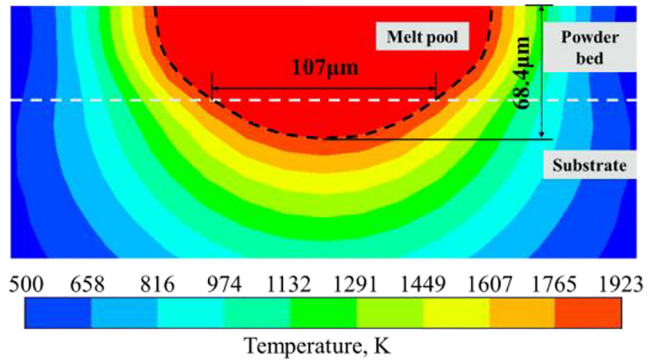

Fig. 5. The cross section of the molten pool for 120 mm/s scanning speed, 50 W laser power and 50 μm powder layer thickness.

accuracy of the numerical simulation model is validated by the experimental results. Second, a series of scan strategies are simulated under different numbers of lasers, scan lengths, scanning directions, sweeping directions and sequences. Finally, the influence of scan strategy on the residual stress is investigated by comparing the simulation results.

Physical model

Physical model and assumption

After irradiated by laser beam, metal powders rapidly form into the molten pool. As the laser beam moving away, the molten pool cools down as a result of heat transfer including the heat conduction to deposited material and powder as well as the convection and radiation to the ambient atmosphere. Inside the molten pool, the Marangoni Effect promotes the flow of high temperature liquid metal to low temperature which accelerates the cooling process. The heat transfer, phase change, microstructure growth and more mechanisms result in the complexity of thermal behavior and mechanical condition. In this section, a transient thermo-mechanical numerical model is established to account for the complexity in the SLM process. In this model, the temperature and the liquid flow fields are first simulated in the thermal model, and then the results are imported to the mechanical model as the thermal load. Note that in this paper, the following four assumptions are made in order to simplify the numerical model:

1. The discrete powder bed is simplified as a homogeneous and continuous media.
2. Fluid in the molten pool is considered to be an incompressible flow of Newtonian fluid.
3. The surface of the deposited layer is considered to be flat.
4. Effects of strains induced by solid-state phase transformation are neglected.

Governing equation

In light of the thermal analysis, the Finite Volume Method (FVM) is adopted to calculate the temperature and flow fields. Based on the above assumptions, the equation of energy conservation is solved in this model, which can be expressed as:

$$\rho c_p \cdot \left(\frac{\partial T}{\partial t} + \mathbf{u}\cdot\nabla T\right) - \nabla\cdot(k\nabla T) = Q - \rho\left(\frac{\partial}{\partial t}\Delta H + \nabla\cdot(\mathbf{u}\Delta H)\right) - q_l \quad (1)$$

where ρ is the density, c_p is the heat capacity, T is the temperature of martial, $\mathbf{u}$ is the velocity of the fluid flow, k is the thermal conductivity, ΔH refers to the latent heat of phase change, q_l is heat loss on the top surface of the powder bed and Q is the volumetric Gaussian heat source. For a given element located at (x, y, z), the heat source $Q(x, y, z)$ can be defined as:

$$Q(x, y, z) = A_p \frac{Pd}{\pi {r_0}^2} \exp\left\{-\frac{d\left[(x - x_l)^2 + (y - y_l)^2\right]}{{r_0}^2}\right\} \cdot I(z) \quad (2)$$

where A_p is the absorption of the powder bed, P refers to the laser power, d is the distribution coefficient of laser beam, r_0 is the radius of the laser beam, (x_l, y_l) is the horizontal location of the laser beam in the coordinate system of workpiece and $I(z)$ refers to the exponential decay in z direction which is expressed as follows [28]:

$$I(z) = A_z \exp(-A_z \cdot |z - z_t|) \quad (3)$$

where A_z is the attenuation coefficient, z_t is the vertical location of the top surface of the processing layer.

To figure out the mechanical response in SLM process, the temperature field is imported into a quasi-static mechanical model based on the Finite Element Method (FEM). The total strain ε_{tot} consists of elastic strain ε_e, thermal strain ε_{th} and plastic strain ε_p shown as follows:

$$\varepsilon_{tot} = \varepsilon_e + \varepsilon_{th} + \varepsilon_p \quad (4)$$

A multilinear isotropic hardening model with Von-Mises yield criterion is used to calculate plastic strain. The elastic stress which is residual stress in the workpiece relative to elastic strain is expressed as:

$$\sigma_e = [D]\cdot\varepsilon_e \quad (5)$$

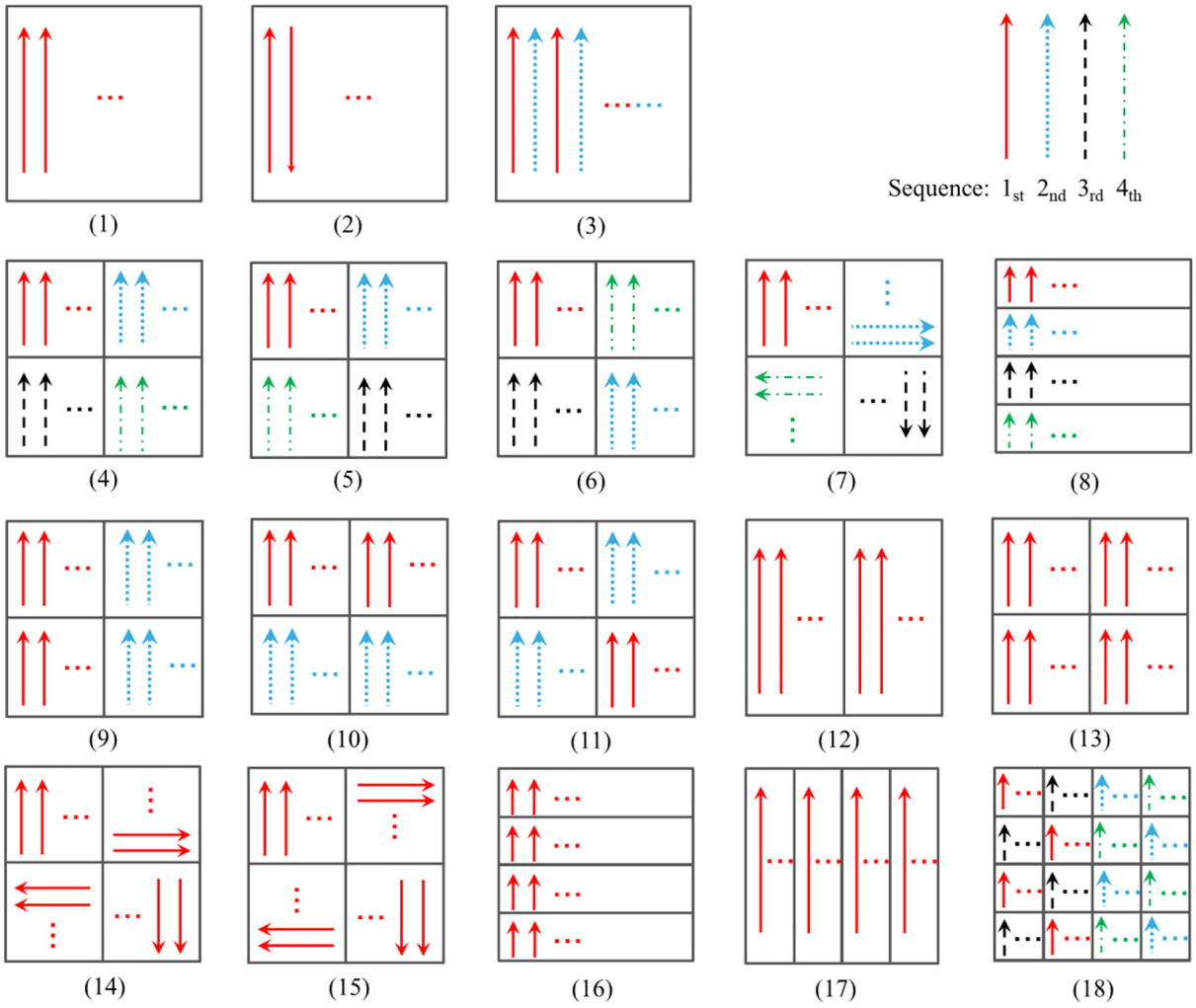

Fig. 6. Schematics of 18 scan strategies: (1) S14A, (2) S14B, (3) S14C, (4) S12A, (5) S12B, (6) S12C, (7) S12D, (8)S11A, (9) S22A, (10) S22B, (11) S22C, (12) S24A, (13) S42A, (14) S42B, (15) S42C, (16) S41A, (17) S44A, (18) S41B.

where $[D]$ is the elastic stiffness matrix. The thermal strain is defined as:

$$\varepsilon_{th} = \int_{T_{ref}}^{T} \alpha_{th} \cdot dT \tag{6}$$

where α_{th} is the coefficient of thermal expansion and T_{ref} is the reference temperature where thermal strain is assumed to be zero.

Boundary conditions

The temperature gradient on the surface of the molten pool contributes to the surface tension gradient, which induces Marangoni Effect. Therefore, the convective flow develops within the molten pool under the effect of Marangoni Effect, gravity and buoyancy. The Marangoni stress τ_m can be defined as [29]:

$$\tau_{mx} = \frac{d\gamma}{dT}\frac{dT}{dx} \quad \tau_{my} = \frac{d\gamma}{dT}\frac{dT}{dy} \tag{7}$$

where τ_{mx} and τ_{my} are Marangoni stress in the × and y direction respectively, γ is the surface tension and $d\gamma/dT$ is called the Marangoni coefficient.

In addition, the temperature-dependent convective and radiative heat flux which is the main heat loss on the top surface is considered in the physical model. The side surfaces of the part and substrate are considered to be heat insulated, and the bottom of the substrate is assumed to be at a fixed temperature which is equal to the ambient temperature. In addition, a fixed surface constraint is applied to the bottom of the substrate for mechanical analysis.

Material properties

To accurately predict the temperature field of workpiece, thermal properties of the metal in different phases should be considered, especially the thermal conductivity of powder and the heat capacity during phase change. The effective thermal conductivity of the powder bed mainly depends on the porosity. The equation of powder thermal conductivity k_p can be expressed as [30]:

$$\frac{k_p}{k_g} = (1-\sqrt{1-\phi})\left(1+\frac{\phi k_r}{k_g}\right) + \sqrt{1-\phi}\left\{\frac{2}{1-\frac{k_g}{k_s}}\left[\frac{1}{1-\frac{k_g}{k_s}}\ln\left(\frac{k_s}{k_g}\right)-1\right]+\frac{k_r}{k_g}\right\} \tag{8}$$

where k_g is the thermal conductivity of the ambient gas in the chamber, Φ is the porosity of the powder bed, k_s is the thermal conductivity of solid metal and k_r is the thermal conductivity of powder induced by radiation, which can be defined as:

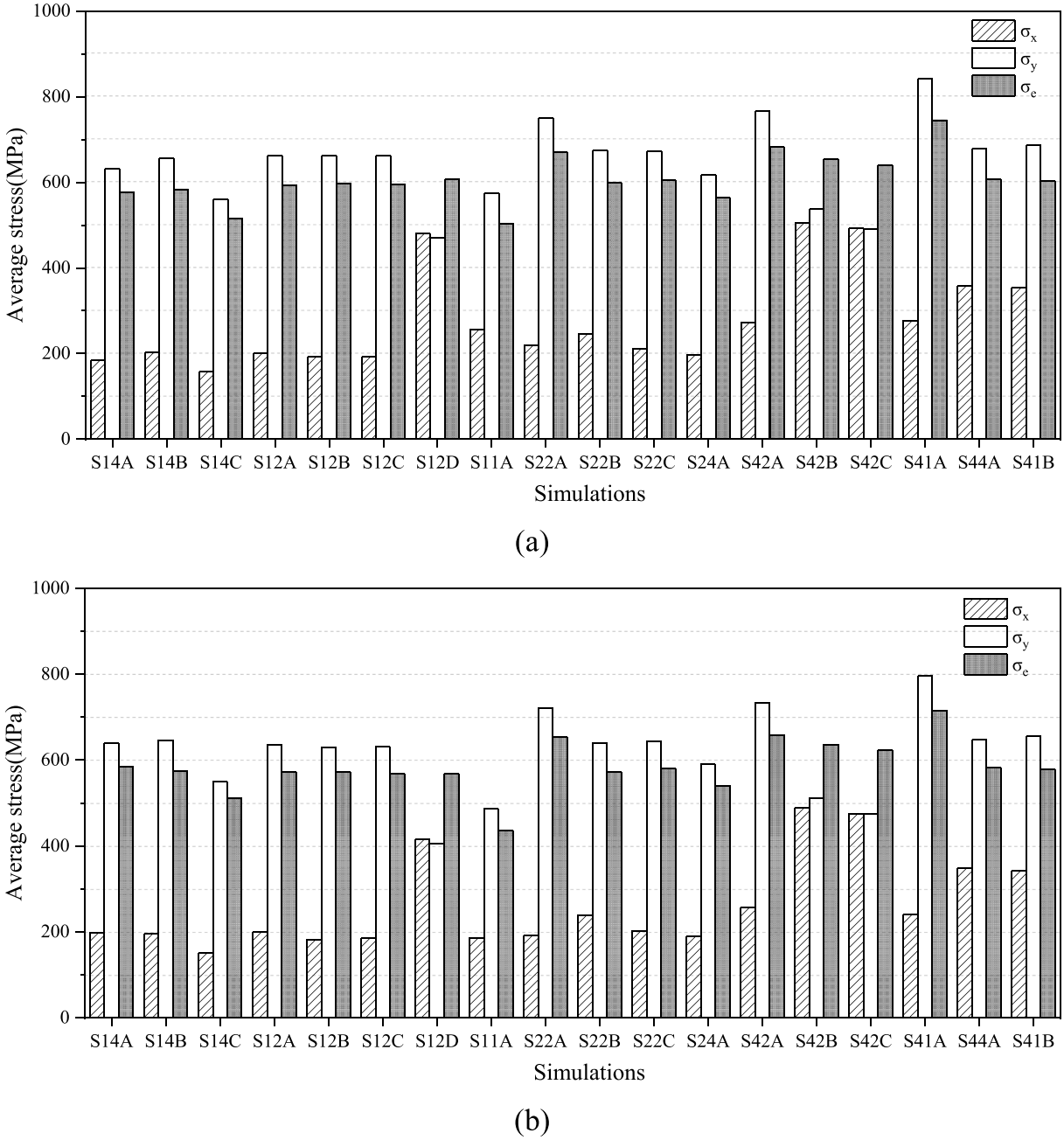

Fig. 7. The average values of σ_x, σ_y and σ_e on (a) the first layer and (b) the second layer.

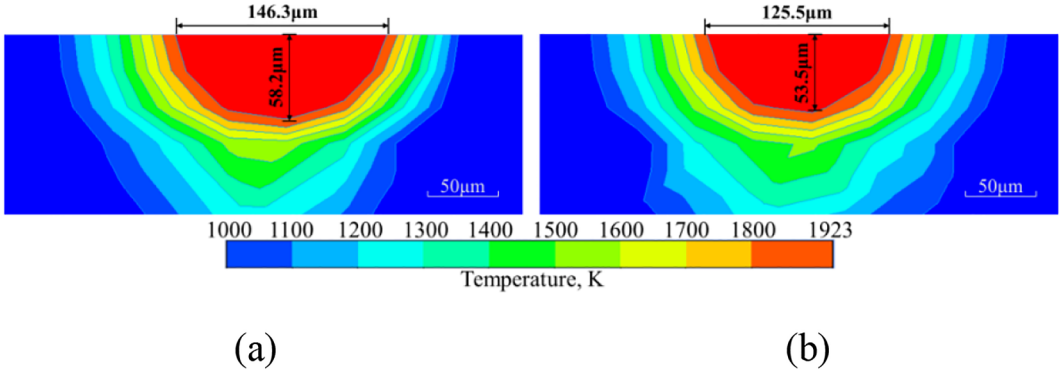

Fig. 8. Cross sections of molten pools in (a) S14A and (b) the second sweep of S14C.

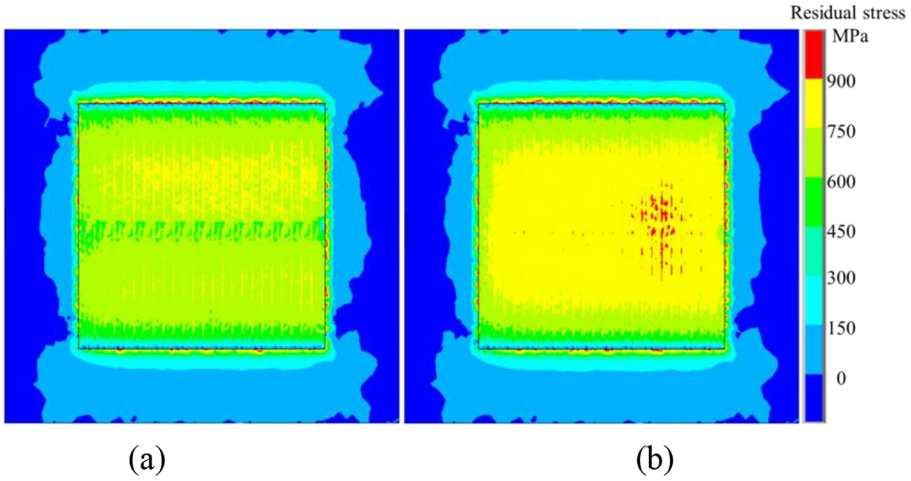

Fig. 9. Surface longitudinal stress fields on the first layers of (a) S12A and (b) S22A.

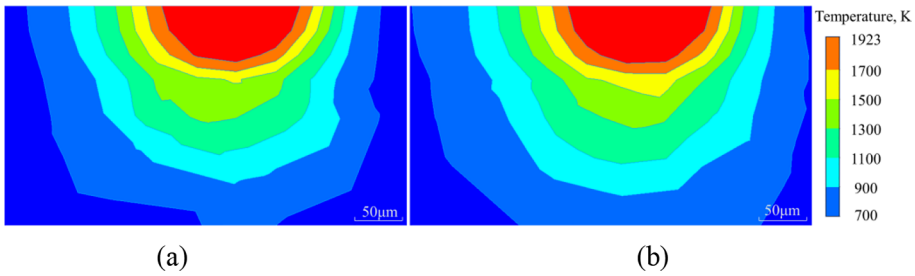

Fig. 10. The cross-sectional temperature distributions of (a) S24A and (b) S44A.

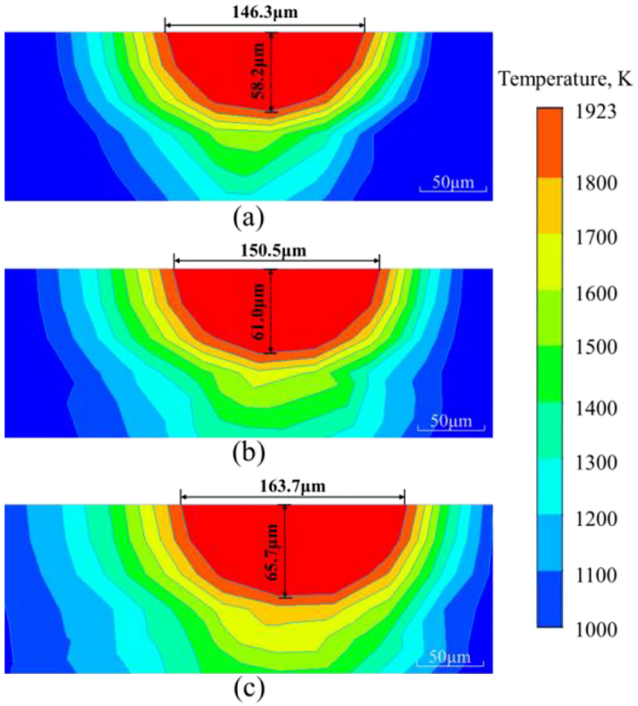

Fig. 11. The cross-sectional temperature distributions of (a) S14A, (b) S12A and (c) S11A.

$$k_r = 4F_0\sigma_r T^3 D_p \tag{9}$$

where F_0 is the radiation view factor which is taken as 1/3, D_p is the average diameter of powder particles.

Due to the large amount of latent heat during phase change, the

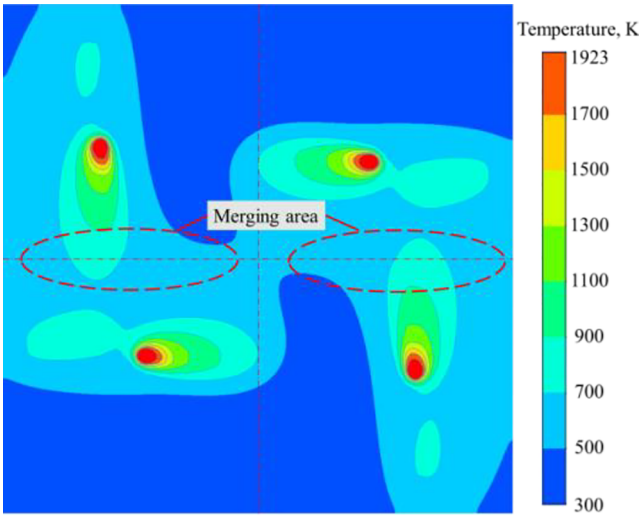

Fig. 12. Surface temperature distribution on the first layers of S42B at 0195 s.

enthalpy of material H and sensible enthalpy h can be defined as:

$$H = h + \theta\cdot\Delta H \; h = h_{ref} + \int_{T_{ref}}^{T} c_p dT \tag{10}$$

where h_{ref} and T_{ref} is the reference enthalpy and the corresponding temperature, θ is the liquid fraction which can be defined as:

$$\theta = \begin{cases} 0 & T < T_s \\ \frac{T - T_s}{T_l - T_s} & T_s < T < T_l \\ 1 & T > T_l \end{cases} \tag{11}$$

where T_s and T_l are the solidification and liquidation temperatures. For the mechanical analysis, the elastic modulus, the yield strength,

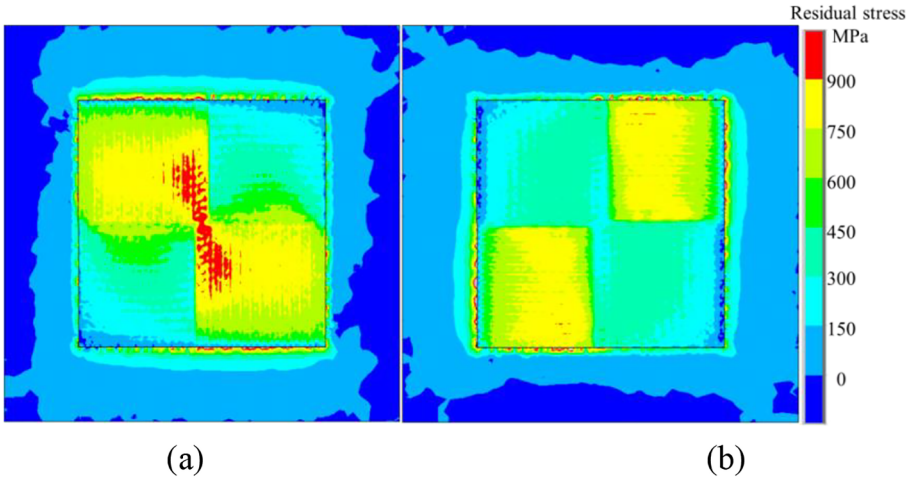

Fig. 13. (a) Longitudinal and (b) transversal residual stress distributions of S42B.

the thermal expansion, the powder stress, the powder strain and liquid metal are assumed to be negligible. Therefore, the birth and death of element method is adopted, which can be used to clear the stresses or strains of deactivated elements [31].

Simulation and validation

Simulation overview

The Computational Fluid Dynamics (CFD) software FLUENT and FEM software ANSYS are used to calculate the temperature field and the stress field, respectively. The simulation process, as shown in Fig. 1, consists of thermal simulation, data conversion and mechanical simulation.

To improve the convergence and accuracy for both thermal and mechanical calculations, the powder bed and the contacted regions of substrate are meshed using hexahedral cells with fine resolution. The rest part of the substrate is meshed with coarse tetrahedral cells in order to save computing time. A User-defined Function (UDF), which is related to both time and temperature, is developed to define thermophysical properties, heat source and laser scan pattern. To distinguish the thermal properties between powder metal and liquid/solid metal, a 3D array is introduced to record the phases of all the powder bed elements. Once the temperature of the powder element reaches melting point, the liquid/solid metal property is assigned to it and the array is updated simultaneously.

Validation

The accuracy of the numerical simulation model is validated by experimental results from the literature [15,32–34]. The molten pool dimensions or maximum temperatures of single-track Ti-6Al-4V with different scanning speeds are generally utilized for verification as shown in Fig. 2 [12,15,26,34].

Temperature-dependent thermal and mechanical properties of Ti-6Al-4V from the published literature are introduced in this simulation [35–37]. For the material in mushy zone, where the temperature is between solidus and liquidus temperature, the liquid fraction θ is introduced to express thermal properties. To restrict the movement of elements in FLUENT, the viscosity of the solid phase is set to be 1 N/(m·s) which is extremely higher than that of the liquid phase.

The laser absorption of the melt pool is assumed to be temperature and phase independent and near-equal to that of solid and powder materials during the SLM process [15,34,35]. To determine the laser absorption and attenuation coefficient, simulations that operate SLM at the substrate Ti-6Al-4V without powder are performed firstly [32]. The SLM processing parameters are shown in Table 1. The laser power is fixed on 50 W and scanning speed varies between 100 mm/s, 200 mm/s and 300 mm/s. Since there is no pre-heat process, the initial temperature of the substrate, the powder bed and the ambient atmosphere are assumed as 300 K. As shown in Fig. 3, the simulation results are consistent with the experimental results under the values of laser absorption 0.47 and attenuation coefficient 5×10^4. The molten pool dimension and the maximum temperature are both within the experimental range. The average error rate between the calculated results and the average experimental results is 1.5%. To further validate the numerical simulation model, simulations of SLM processes with 30 μm thick Ti-6Al-4V powder reported by Chen are performed and the results are compared with those of experiments [34]. The SLM processing parameters are shown in Table 1. By altering the scanning speed between 125 mm/s, 200 mm/s and 250 mm/s with constant laser power, the linear heat inputs range from 200 J/mm to 400 J/mm that are consistent with experimental conditions. As shown in Fig. 4, the simulation results agree well with the experimental results. The maximum relative error for the molten pool width and depth are 7.18% and 15.3%, respectively. Thus, it can be concluded that the calculated temperature field can be regarded as thermal load for the residual stress calculation.

Scan strategy

The Ti-6Al-4V SLM process with multiple tracks and two layers is simulated using the validated numerical model. The dimensions of the powder bed and the substrate are $5 \times 5 \times 0.1$ mm^3 and $8 \times 8 \times 1$ mm^3 respectively. As reported by Yadroitsev, the optimal scanning speed is 120 mm/s with 50 W laser and 50 μm powder layer thickness [32]. According to the simulation result, shown in Fig. 5, the depth of the melt pool is 68.4 μm which is higher than the powder layer thickness. It means that the powder bed can be fully penetrated. In addition, to achieve high relative density, the hatch spacing is selected as 100 μm that is shorter than the width of the intersection of the melt pool and the substrate (107 μm). The other simulation parameters are shown in Table 1.

There are 18 simulations with various scan strategies performed in this paper where the first and second layers are fabricated in the same scan strategy. The schematics of these scan strategies with different numbers of lasers, scan lengths, scanning directions, sweeping directions and sequences are shown in Fig. 6. The direction of the arrow represents the scanning direction of the laser, and the sweeping direction is perpendicular to the scanning direction and points to the ellipsis. Different colors and line styles of arrows indicate sequences in the simulation. Taking case S14A as an example, the ‘S’ stands for ‘scan

strategy'; the '1′ means that the number of lasers is 1; the '4′ represents that the length of scan track is 4 times of the minimum scan length; the 'A' is used to distinguish other factors, such as scanning direction, sweeping direction and scanning sequence.

Results and discussion

The powder bed is rapidly heated by the laser beam and the heat transfer within the material is relatively slow, hence a steep temperature gradient is developed in the workpiece leading to the formation of the molten pool. Under the effect of plastic deformation during the heating and cooling process, residual stresses develop in the heated zone around the melton pool. Meanwhile, for the molten pool (fusion zone), no residual stress or plastic strain develops in melting state due to the fluidity of molten metal. However, the solidification and the shrinkage of the molten pool lead to tensile stress as temperature drops down. These two mechanisms determine the formation of residual stress in the workpiece [7].

To detail the effect of scan strategy on residual stress, the transversal stress σ_x, the longitudinal stress σ_y and the equivalent stress σ_e of 64 points are investigated, which are uniformly distributed on the top surface of each layer. As shown in Fig. 7, the average values of σ_x, σ_y and σ_e have been calculated for all the cases.

In general, residual stresses of the second layer are slightly lower than those of the first layer. As the horizontal dimension of the deposited layer is smaller than that of the substrate, the first deposited layer is easier to deform than the substrate [14]. As a result, less plastic strains and residual stresses are developed in the second layer. Since residual stress trend of the second layer is similar to the first layer, the discussions below are mainly focused on the results of first layer.

Two-zone technique and scanning direction

Since residual stresses of S14C are lower than those of S14A or S14B in both longitudinal and transversal directions, as shown in Fig. 7 (a), it can be concluded that "two-zone technique" scan strategy effective in lowering the residual stress. In the first sweep of S14C, the deposited tracks have fewer constraints from adjacent tracks because of large hatch space. This results in a relatively low residual stress. During the second sweep, scan tracks are surrounded by solidified materials with higher thermal conductivity, the heat accumulation and the dimension of molten pool will decrease. As shown in Fig. 8, the width of molten pool in the second sweep of S14C (125.5 μm) is 14.2% shorter than that of S14A (146.3 μm), and the depth of S14C (53.5 μm) is 8% shorter than that of S14A (58.2 μm). Since larger molten pool results in more volume shrinkage after solidification, the residual stress in S14A is higher than that in S14C in the second sweep. Furthermore, it can be seen that altering scanning directions has little effect on the average residual stress, since the average σ_e stress of S14B is similar to that of S14A.

Number of lasers

Comparing cases with same scan patterns, excluding case S22A, there are no significant differences in average σ_e stresses when the number of lasers increases from 1 to 2. This is due to the fact that lasers are relatively far away in the double-laser scanning process that avoids the heat concentration effect. However, as shown in Fig. 7 (a), the average longitudinal stress of case S22A is 13.3% higher than that of case S12A. Since the scanning vectors of the two lasers are collinear, scan tracks merge on the longitudinal direction in S22A. As a result, both the head of the upper scan track and the end of the bottom one are obstructed in shrinkage that induces high residual stresses. The residual stress distribution is continuous at scan track joints in S22A (Fig. 9 (b)), which is different from that of S12A (Fig. 9 (a)). This effect is equivalent to an increase in the scan track which is called the scan track extension effect (STEE) in this article.

The results in Fig. 7 (a) show that the residual stress becomes significantly high when the number of lasers comes to 4, for instance, the average equivalent residual stress of S42B is 9.0% higher than that of S22B. Taking S22A and S24A as examples, the cross-sectional temperature distributions of S24A and S44A are shown in Fig. 10. It can be seen that the heated zone round the molten pool of S24A (Fig. 10 (a)) is smaller than that of S44A (Fig. 10 (b)) due to the shorter relative distance between lasers in S44A. Thus, the average longitudinal stress of S44A is 9.8% higher than that of S24A.

Scan length

With the scan length decreasing for the single laser SLM process, the average longitudinal stress increases slightly from 632.3 MPa (S14A) to 661.4 MPa (S12A) and then drops dramatically to 575.2 MPa (S11A). Also, the multi-laser process has the same trend. In order to investigate the effect of scan length on residual stress, S14A, S12A and S11A are taken as examples. Since the scan length decreases, the constraints on the scan track during the cooling process reduce that effectively mitigates residual stresses. In addition, it can be seen by the cross-sectional temperature distributions of S14A, S12A and S11A which are shown in Fig. 11 that the temperature gradient decreases with the scan length. However, reducing scan length leads to a larger dimension of molten pool, resulting in larger scale shrinkage and higher residual stress for fusion zone.

Based on the above analysis, it can be found that the changes of constraints on scan tracks, temperature gradient and molten pool sizes resulted from varying scan length have opposite effects on residual stresses. This explains the phenomenon that the longitudinal residual stress has no direct correlation with the scan length.

On the transversal direction, it is clear that the transversal residual stress increases with the decrease of scan length, since average σ_x stresses of S14A, S12A and S11A increase successively. The fact is that the heated zone perpendicular to scan vector increases with the decrease of time interval that induces more plastic deformations and higher residual stresses.

Scanning sequence and sweeping direction

From Fig. 7 (a), there are no obvious differences between residual stresses of S12A, S12B and S12C. It can be concluded that the scanning sequence has little effect on residual stress for the single laser process. However, residual stress is sensitive to scanning sequence under the condition of multi-laser scanning. The average σ_e stress of S22A is 11.9% higher than that of S22B and the average σ_e stress of S41A is 22.8% higher than that of S41B. This is because scanning vectors are collinear in both S22A and S41A that results in the STEE. Therefore, it is significant for multi-laser SLM process to reduce residual stress by carefully planning scanning sequence to mitigate the STEE between islands. Although 4 lasers have been employed, the average σ_e stress of S41B is close to that of cases with double-laser scan strategies.

From results of S12A, S12D, S42A and S42B, it can be indicated that varying sweeping direction is beneficial for residual stresses to be evenly distributed in both longitudinal and transversal directions. As shown in Fig. 7 (a), there is no big difference in the average Von Mises stress between S12A and S12D. This indicates that varying sweeping direction for the single laser SLM process has little effect on the magnitude of residual stress. However, the average σ_e stress of S42B is 4.1% lower than S42A. Hence, it is significant to apply appropriate sweeping directions to reduce residual stresses for the multi-laser scan strategy. Furthermore, the mergence of melted regions between upper and bottom islands in S42B, as shown in Fig. 12, promotes constraints on scan tracks. As a result, the distributions of longitudinal and transversal residual stresses are not rotated symmetric, as shown in Fig. 13, and the longitudinal average stress is 6.6% higher than transversal one. Through varying sweeping directions to mitigate merging effect among

the islands, the average σ_e stress of S42C is reduced by 2.2%.

Conclusion

A 3D thermo-mechanical model where the temperature and phase dependent properties of Ti-6Al-4V, phase change and convective flow are considered is developed to simulate the SLM process. The numerical model is first validated by experimental results and then used to calculate temperature fields and stress fields with different scan strategies. The major findings are summarized below:

(1) The "two-zone technique" scan strategy has shown a reduction in the residual stress by 10.6% in comparison to the traditional successive scan strategy.
(2) The residual stress is significantly higher as the number of lasers increases to four, which is due to more heat input.
(3) The residual stress is sensitive to the scan length for both the single-laser scan strategy and the multi-laser scan strategy, but there is no consistent correlation between them. With the scan length decreasing in the single laser SLM process, the average longitudinal stress first increases slightly by 4.6% and then decreases dramatically by 13.0%.
(4) For the multi-laser SLM process, the scanning sequence and the sweeping direction are two crucial factors in controlling residual stress. After changing the scanning sequence of S41A, the average equivalent stress of S41B reduces by 19.0%. Meanwhile, by altering the sweeping direction of S42A, the average equivalent stress of S42B decreases by 6.2%.

Acknowledgement

This work is supported by the Fundamental Research Funds for the Central Universities of China (2016-JL-012).

References

[1] Huang Y, Yang LJ, Du XZ, Yang YP. Finite element analysis of thermal behavior of metal powder during selective laser melting. Int J Therm Sci 2016;104:146–57.
[2] Wang X, Xu S, Zhou S, Xu W, Leary M, Choong P, et al. Topological design and additive manufacturing of porous metals for bone scaffolds and orthopaedic implants: A review. Biomaterials 2016;83:127–41.
[3] Frazier WE. Metal additive manufacturing: a review. J Mater Eng Perform 2014;23(6):1917–28.
[4] Zekovic, S., Dwivedi, R., & Kovacevic, R. (2005, August). Thermo-structural finite element analysis of direct laser metal deposited thin-walled structures. In Proceedings SFF Symposium,. Austin, TX.
[5] Baumers M, Tuck C, Wildman R, Ashcroft I, Hague R. Shape complexity and process energy consumption in electron beam melting: A case of something for nothing in additive manufacturing? J Ind Ecol 2017;21(S1):S157–67.
[6] Lewis GK, Schlienger E. Practical considerations and capabilities for laser assisted direct metal deposition. Mater Des 2000;21(4):417–23.
[7] Mercelis P, Kruth JP. Residual stresses in selective laser sintering and selective laser melting. Rapid prototyping journal 2006;12(5):254–65.
[8] DebRoy T, Wei HL, Zuback JS, Mukherjee T, Elmer JW, Milewski JO, et al. Additive manufacturing of metallic components–process, structure and properties. Prog Mater Sci 2018;92:112–224.
[9] Rangaswamy P, Griffith ML, Prime MB, Holden TM, Rogge RB, Edwards JM, et al. Residual stresses in LENS® components using neutron diffraction and contour method. Mater Sci Eng, A 2005;399(1–2):72–83.
[10] Amine T, Newkirk JW, Liou F. Investigation of effect of process parameters on multilayer builds by direct metal deposition. Appl Therm Eng 2014;73(1):500–11.
[11] Price S, Cooper K, Chou K. August). Evaluations of temperature measurements by near-infrared thermography in powder-based electron-beam additive manufacturing. Austin, TX: University of Texas; 2012. p. 761–73.
[12] Parry L, Ashcroft IA, Wildman RD. Understanding the effect of laser scan strategy on residual stress in selective laser melting through thermo-mechanical simulation. Addit Manuf 2016;12:1–15.
[13] Panda BK, Sahoo S. Thermo-mechanical modeling and validation of stress field during laser powder bed fusion of AlSi10Mg built part. Results Phys 2019;12:1372–81.
[14] Zhao X, Iyer A, Promoppatum P, Yao SC. Numerical modeling of the thermal behavior and residual stress in the direct metal laser sintering process of titanium alloy products. Addit Manuf 2017;14:126–36.
[15] Masoomi M, Thompson SM, Shamsaei N. Laser powder bed fusion of Ti-6Al-4V parts: Thermal modeling and mechanical implications. Int J Mach Tools Manuf 2017;118:73–90.
[16] Ren K, Chew Y, Fuh JYH, Zhang YF, Bi GJ. Thermo-mechanical analyses for optimized path planning in laser aided additive manufacturing processes. Mater Des 2019;162:80–93.
[17] Mukherjee T, Zhang W, DebRoy T. An improved prediction of residual stresses and distortion in additive manufacturing. Comput Mater Sci 2017;126:360–72.
[18] Carter LN, Martin C, Withers PJ, Attallah MM. The influence of the laser scan strategy on grain structure and cracking behaviour in SLM powder-bed fabricated nickel superalloy. J Alloy Compd 2014;615:338–47.
[19] Simonelli M, Tse YY, Tuck C. On the texture formation of selective laser melted Ti-6Al-4V. Metall Mater Trans A 2014;45(6):2863–72.
[20] Aboulkhair NT, Everitt NM, Ashcroft I, Tuck C. Reducing porosity in AlSi10Mg parts processed by selective laser melting. Addit Manuf 2014;1:77–86.
[21] Ma L, Bin H. Temperature and stress analysis and simulation in fractal scanning-based laser sintering. Int J Adv Manuf Technol 2007;34(9–10):898–903.
[22] Cheng B, Shrestha S, Chou K. Stress and deformation evaluations of scanning strategy effect in selective laser melting. Addit Manuf 2016;12:240–51.
[23] Ali H, Ghadbeigi H, Mumtaz K. Effect of scanning strategies on residual stress and mechanical properties of Selective Laser Melted Ti6Al4V. Mater Sci Eng, A 2018;712:175–87.
[24] Wu AS, Brown DW, Kumar M, Gallegos GF, King WE. An experimental investigation into additive manufacturing-induced residual stresses in 316L stainless steel. Metall Mater Trans A 2014;45(13):6260–70.
[25] Lu Y, Wu S, Gan Y, Huang T, Yang C, Junjie L, et al. Study on the microstructure, mechanical property and residual stress of SLM Inconel-718 alloy manufactured by differing island scanning strategy. Opt Laser Technol 2015;75:197–206.
[26] Liu B, Li BQ, Li Z, Bai P, Wang Y, Kuai Z. Numerical investigation on heat transfer of multi-laser processing during selective laser melting of AlSi10Mg. Results Phys 2019;12:454–9.
[27] Zhang C, Zhu H, Hu Z, Zhang L, Zeng X. A comparative study on single-laser and multi-laser selective laser melting AlSi10Mg: defects, microstructure and mechanical properties. Mater Sci Eng, A 2019;746:416–23.
[28] Yadroitsev I, Krakhmalev P, Yadroitsava I. Hierarchical design principles of selective laser melting for high quality metallic objects. Addit Manuf 2015;7:45–56.
[29] Raghavan A, Wei HL, Palmer TA, DebRoy T. Heat transfer and fluid flow in additive manufacturing. J. Laser Appl 2013;25(5):1207–16.
[30] Safdar S, Li L, Sheikh MA. Numerical analysis of the effects of non-conventional laser beam geometries during laser melting of metallic materials. J Phys D Appl Phys 2007;40(2):593.
[31] Roberts IA, Wang CJ, Esterlein R, Stanford M, Mynors DJ. A three-dimensional finite element analysis of the temperature field during laser melting of metal powders in additive layer manufacturing. Int J Mach Tools Manuf 2009;49(12–13):916–23.
[32] Yadroitsev I, Krakhmalev P, Yadroitsava I. Selective laser melting of Ti6Al4V alloy for biomedical applications: Temperature monitoring and microstructural evolution. J Alloy Compd 2014;583:404–9.
[33] Ali H, Ghadbeigi H, Mumtaz K. Residual stress development in selective laser-melted Ti6Al4V: A parametric thermal modelling approach. Int J Adv Manuf Technol 2018;97(5–8):2621–33.
[34] Chen C, Yin J, Zhu H, Xiao Z, Zhang L, Zeng X. Effect of overlap rate and pattern on residual stress in selective laser melting. Int J Mach Tools Manuf 2019;145:103433.
[35] Zhang T, Li H, Liu S, Shen S, Xie H, Shi W, et al. Evolution of molten pool during selective laser melting of Ti–6Al–4V. J Phys D Appl Phys 2018;52(5):055302.
[36] Mills KC. Recommended values of thermophysical properties for selected commercial alloys. Woodhead Publishing; 2002.
[37] Rangaswamy, P. (2000). HIGH TEMPERATURE STRESS ASSESSMENT IN SCS-6/TI-6A1-4V COMPOSITE USING NEUTRON DIFFRACTION AND FINITE ELEMENT MODELING (No. LA-UR-00-5277). Los Alamos National Lab., Los Alamos, NM (US).
[38] Sih SS, Barlow JW. The prediction of the emissivity and thermal conductivity of powder beds. Part Sci Technol 2004;22(4):427–40.